

USING REAL AND SIMULATED MEASUREMENTS OF THE THERMAL SUNYAEV-ZEL'DOVICH EFFECT TO CONSTRAIN MODELS OF AGN FEEDBACK

ALEXANDER SPACEK^{1,2}, MARK RICHARDSON^{3,4}, EVAN SCANNAPIECO¹

¹School of Earth and Space Exploration, Arizona State University, PO Box 876004, Tempe, AZ 85287, USA

²Los Alamos National Laboratory, PO Box 1663, Los Alamos, NM 87545, USA

³Sub-department of Astrophysics, University of Oxford, Keble Road, Oxford OX1 3RH, UK and

⁴Astrophysics Department, American Museum of Natural History, Central Park West at 79th Street, New York, NY 10024, USA

Draft version June 15, 2022

ABSTRACT

Energetic feedback from active galactic nuclei (AGNs) is difficult to observe, but often used in simulations to resolve several outstanding issues in galaxy formation. Here we derive new constraints on AGN feedback by comparing observations and simulations of the thermal Sunyaev-Zel'dovich (tSZ) effect, which causes spectral distortions in the cosmic microwave background with signal strengths that are proportional to the total energy deposited into the medium surrounding large galaxies. We draw on observational results presented in Spacek et al. (2016, 2017) who used data from the South Pole Telescope (SPT) and Atacama Cosmology Telescope (ACT) to measure the tSZ signal from $\geq 10^{11} M_{\odot}$ and ≥ 1 Gyr galaxies in the redshift ranges of $z=0.5\text{--}1.0$ (low- z) and $z=1.0\text{--}1.5$ (high- z). Using two large-scale cosmological hydrodynamical simulations, one with AGN feedback (Horizon-AGN) and one without (Horizon-NoAGN), we extract simulated tSZ measurements around a population of galaxies equivalent to those observed. We find that the Horizon-AGN results only differ from the SPT measurements at levels of 0.4σ at low- z and 0.5σ at high- z , but they differ from the ACT measurements at levels of 6.9σ at low- z and 14.6σ at high- z . The Horizon-NoAGN results provide a slightly worse fit to the SPT measurements at levels of 1.8σ at low- z and 0.6σ at high- z , but a drastically better match to the ACT measurements at levels of 0.8σ at low- z and 1.9σ at high- z . We conclude that, while the lower-mass ($\lesssim 5 \times 10^{11} M_{\odot}$) SPT results show a hint of AGN feedback energy, the higher-mass ($\gtrsim 5 \times 10^{11} M_{\odot}$) ACT results show significantly less energy than predicted in the simulation including feedback, indicating that AGN feedback may be milder than often predicted.

1. INTRODUCTION

Galaxies are some of the most prominent objects in the Universe, but the processes governing their formation and evolution are surprisingly uncertain. Although early models favored hierarchical galaxy evolution, in which progressively larger galaxies form stars at later times (e.g. Rees & Ostriker 1977; White & Frenk 1991), an increasing amount of observational evidence reveals a more complex history. For example, at later times there is the appearance of cosmic ‘downsizing’ (e.g. Cowie et al. 1996). Since $z \approx 2$ the typical mass of star-forming galaxies has decreased by a factor of ≈ 10 or more (Drory & Alvarez 2008). A similar history is observed for AGNs, whose typical luminosities have decreased by as much as a factor of ≈ 1000 since $z \approx 2$ (Hopkins et al. 2007). This observed concurrent downsizing trend of both galaxies and AGNs, combined with other well-known relationships between supermassive black holes and their host galaxies (e.g. Shankar et al. 2016), points to a mechanism likely affecting both the small scale of the supermassive black hole ($\lesssim 1$ ly) and the large scale of the galaxy ($\gtrsim 100$ kly).

One such mechanism is feedback during the AGN phase of supermassive black hole evolution (e.g. Scannapieco & Oh 2004; Granato et al. 2004; Croton et al. 2006). AGNs are energetic enough to drive out enormous, powerful radio jets, as well as extremely luminous radiative winds, causing energetic outflows through the host galaxy. This feedback has the potential to blow out and heat up gas within and around the galaxy, prevent-

ing both further star formation in the galaxy and further accretion onto the supermassive black hole. Incorporating AGN feedback into numerical galaxy evolution models has been shown to be very effective in reproducing observed galaxy trends (e.g. Sijacki et al. 2007; Lapi et al. 2014; Kaviraj et al. 2017), including downsizing (e.g. Thacker et al. 2006; Hirschmann et al. 2012). However, the specific details of AGN feedback remain uncertain because precise details are very difficult to measure (e.g. Fabian 2012).

One of the most promising methods for directly measuring the impact of AGN feedback on galaxies and clusters is by looking at anisotropies in the cosmic microwave background (CMB) photons passing through hot, ionized gas. If the gas is moving with a bulk velocity, there will be frequency-independent fluctuations in the CMB temperature known as the kinematic Sunyaev-Zel'dovich effect (kSZ; Sunyaev & Zeldovich 1972), which can be used to detect the profile of ionized gas within dark matter halos, providing information on where hot gas is located around galaxies. This method is becoming increasingly promising, with some of the first detections of the kSZ effect in galaxy clusters made recently by stacking CMB observations with Planck (Planck Collaboration et al. 2016), the South Pole Telescope (SPT) (Soergel et al. 2016), and the Atacama Cosmology Telescope (ACT) (Schaan et al. 2016).

Additionally, if the gas is sufficiently heated, there will be redshift-independent fluctuations in the CMB temperature known as the thermal SZ (tSZ) effect, which

can be integrated over a region of the sky to give a direct measurement of the gas thermal energy (e.g. Scannapieco et al. 2008). Measurements of the tSZ effect have been very useful in detecting massive galaxy clusters (e.g. Reichardt et al. 2013). Simulations have also shown that the tSZ effect around galaxies can be effective in distinguishing between models of AGN feedback (e.g. Chatterjee et al. 2008; Scannapieco et al. 2008).

Significant observational work has already been done to try and measure the tSZ effect around galaxies and AGNs. For example, Chatterjee et al. (2010) used data from the Wilkinson Microwave Anisotropy Probe and Sloan Digital Sky Survey (SDSS) around both quasars and galaxies to find a tentative tSZ signal suggesting AGN feedback; Hand et al. (2011) used data from SDSS and ACT to find a significant tSZ signal around galaxies; Gralla et al. (2014) used the ACT to find a significant tSZ signal around AGNs; Greco et al. (2015) used SDSS and Planck to find a significant tSZ signal around galaxies; Ruan et al. (2015) used SDSS and Planck to find significant tSZ signals around both quasars and galaxies; Crichton et al. (2016) used SDSS and ACT to find a significant tSZ signal around quasars; and Hojjati et al. (2016) used data from Planck and the Red Cluster Sequence Lensing Survey to find a tSZ signal suggestive of AGN feedback.

Additionally, recent measurements have been made around quiescent, moderate redshift elliptical galaxies (Spacek et al. 2016, 2017, hereafter Papers I and II), where a signal due to AGN feedback is expected (e.g. Scannapieco et al. 2008). The signal is very faint, however, so measurements from a large number of galaxies must be stacked. In Paper I, we performed this type of stacking analysis using the VISTA Hemisphere Survey (VHS) and Blanco Cosmology Survey (BCS) along with the 2011 SPT data release, finding a 3.6σ signal, hinting at non-gravitational heating based on simple energy models. In Paper II, we used the Sloan Digital Sky Survey (SDSS) and Wide-Field Infrared Survey Explorer (WISE) along with the 2008/2009 ACT data, finding a 1.5σ signal consistent with gravitational-only heating based on the same simple energy models.

Directly measuring the energy and distribution of hot gas around galaxies can only reveal so much about the specific physical mechanisms resulting in the observations. In order to place constraints on AGN feedback and other non-gravitational heating processes, it is necessary that observational work be complimented by accurate, detailed simulations. There is a rich history of simulations of the Sunyaev Zel'dovich effect (Scaramella et al. 1993; Hobson & Magueijo 1996; da Silva et al. 2000; Refregier et al. 2000; Springel et al. 2001; Seljak et al. 2001; Zhang et al. 2002; Roncarelli et al. 2007) and of complementing tSZ measurements and AGN feedback with simulations. For example, both Scannapieco et al. (2008) and Chatterjee et al. (2008) used large-scale cosmological simulations to give predictions for measuring AGN feedback with the tSZ effect; Cen & Safarzadeh (2015) used simulations to investigate the feedback energies from quasars and their implications for tSZ measurements; Hojjati et al. (2015) used large-scale cosmological simulations to estimate AGN feedback effects on cross-correlation signals between gravitational lensing and tSZ measurements; and Dolag et al. (2016) used large-scale

simulations to study the impact of structure formation and evolution with AGN feedback on tSZ measurements.

In this work, we use the large-scale cosmological simulations Horizon-AGN and Horizon-noAGN, which are simulations with and without AGN feedback, respectively (Dubois et al. 2012, 2014; Kaviraj et al. 2015, 2017), to compliment the work done in Papers I and II. We investigate a similar population of moderate redshift, quiescent elliptical galaxies and simulate their tSZ measurements. We then use their measurement distribution and stacking statistics to give insight into the previous observational results. These Horizon simulations have a comoving volume of $(100 \text{ Mpc}/h)^3$, 1024^3 dark matter particles, and a minimum cell size of 1 physical kpc. This allows for a large enough population of our galaxies of interest to make robust tSZ measurements, since such high redshift, massive, elliptical galaxies are generally uncommon.

The structure of this paper is as follows: in Section 2, we discuss the tSZ effect and various models of AGN feedback. In Section 3, we discuss the Horizon-AGN simulation. In Section 4, we discuss how we select and measure the tSZ effect around the simulated galaxies. In Section 5, we give the parameters and measurements of our selected galaxies. In Section 6, we discuss implications for our results in regard to Papers I and II, Horizon-AGN, and tSZ measurements of AGN feedback in general.

Throughout this work, we use a Λ Cold Dark Matter cosmological model with parameters following the Horizon simulations: $h = 0.704$, $\Omega_0 = 0.272$, $\Omega_\Lambda = 0.728$, and $\Omega_b = 0.0455$, where h is the Hubble constant in units of $100 \text{ km s}^{-1} \text{ Mpc}^{-1}$, and Ω_0 , Ω_Λ , and Ω_b are the total matter, vacuum, and baryonic densities, respectively, in units of the critical density.

2. THE TSZ EFFECT

When CMB photons pass through hot, ionized gas, inverse Compton scattering between the photons and electrons causes the photons to gain energy, and some of these photons are scattered along our line of sight. The resulting shift in the CMB spectrum has a distinctive frequency dependence, with a weaker signal below, and a stronger signal above, 217.6 GHz. This is the frequency where the tSZ effect is null; measurements near 217.6 GHz can be scaled to other frequencies and subtracted to remove contaminating (i.e. non-tSZ effect) signal. The nonrelativistic change in the CMB temperature ΔT as a function of frequency ν due to the tSZ effect is

$$\frac{\Delta T}{T_{\text{CMB}}} = y \left(x \frac{e^x + 1}{e^x - 1} - 4 \right). \quad (1)$$

Here, $T_{\text{CMB}} = 2.725 \text{ K}$ is the observed CMB temperature today, x is a dimensionless frequency given by $x \equiv \frac{h\nu}{kT_{\text{CMB}}} = \frac{\nu}{56.81 \text{ GHz}}$, h is the Planck constant, k is the Boltzmann constant, and the dimensionless Compton- y parameter is defined as

$$y \equiv \int dl \sigma_T \frac{n_e k (T_e - T_{\text{CMB}})}{m_e c^2}, \quad (2)$$

where σ_T is the Thomson cross section, m_e is the electron mass, c is the speed of light, n_e is the electron number density, T_e is the electron temperature, and the integral is performed over the line-of-sight distance l .

When observing the tSZ effect on the sky, a useful quantity is the angularly integrated Compton- y parameter, Y , given by

$$Y \equiv l_{\text{ang}}^2 \int y(\theta) d\theta, \quad (3)$$

where l_{ang} is the angular diameter distance. For the SPT 150 GHz parameters from Paper I, this is $Y_{\text{SPT}} = 2.7 \times 10^{-8} \text{ Mpc}^2 E_{60}$, where E_{60} is the total line-of-sight gas thermal energy E_{therm} in units of 10^{60} erg. For the ACT 148 GHz parameters from Paper II, this is $Y_{\text{ACT}} = 2.9 \times 10^{-8} \text{ Mpc}^2 E_{60}$. The values are slightly different due to the different frequency sensitivities and beam profiles of the two telescopes. Y can additionally be scaled and written as

$$\tilde{Y} \equiv \frac{Y}{l_{\text{ang}}^2} \times E^{-2/3} \times \left(\frac{l_{\text{ang}}}{500 \text{ Mpc}} \right)^2, \quad (4)$$

where $E(z) \equiv \sqrt{\Omega_0(1+z)^3 + \Omega_\Lambda}$ is the Hubble parameter. It often appears this way in the literature (e.g. Planck Collaboration et al. 2013; Greco et al. 2015; Ruan et al. 2015; Crichton et al. 2016).

In Papers I and II, we used simple models of heating due to gravitation and AGN feedback to compare with observations. For gravity, we assumed that as gas collapses and virializes along with an encompassing spherical halo of dark matter, it is shock-heated to a virial temperature T_{vir} . For isothermal gas, this gives a total thermal energy of

$$\begin{aligned} E_{\text{therm,gravity}} &= \frac{3kT_{\text{vir}}}{2} \frac{\Omega_b}{\Omega_0} \frac{M}{\mu m_p} \\ &= 1.5 \times 10^{60} \text{ erg } M_{13}^{5/3} (1+z), \end{aligned} \quad (5)$$

where m_p is the proton mass, $\mu = 0.62$ is the average particle mass in units of m_p , and M_{13} is the mass of the halo in units of $10^{13} M_\odot$. The relation between halo mass and stellar mass is derived from Ferrarese (2002) and Marconi & Hunt (2003) and given by $M_{\text{stellar}} = 2.8_{-1.4}^{+2.4} \times 10^{10} M_\odot M_{13}^{5/3} (1+z)^{5/2}$. Incorporating this gives

$$\begin{aligned} E_{\text{therm,gravity}} &= \\ 5.4_{-2.9}^{+5.4} \times 10^{60} \text{ erg } \frac{M_{\text{stellar}}}{10^{11} M_\odot} (1+z)^{-3/2}. \end{aligned} \quad (6)$$

This is the total thermal energy expected around a galaxy of stellar mass M_{stellar} ignoring both radiative cooling, which will decrease E_{therm} , and AGN feedback, which will increase it.

For AGN feedback, we used the simple model described in Scannapieco & Oh (2004), where the black hole emits energy at the Eddington luminosity, $L_{\text{Edd}} = 1.26 \times 10^{38} (M_{\text{BH}}/M_\odot) \text{ erg s}^{-1}$ (e.g. Shankar et al. 2013), for a time $0.035 t_{\text{dynamical}}$, with $t_{\text{dynamical}} \equiv R_{\text{vir}}/v_c = 2.6 \text{ Gyr } (1+z)^{-3/2}$, and the gas is heated by a fraction ϵ_k of the total bolometric luminosity of the AGN. This gives

$$\begin{aligned} E_{\text{therm,feedback}} &= \\ 4.1 \times 10^{60} \text{ erg } \epsilon_{k,0.05} \frac{M_{\text{stellar}}}{10^{11} M_\odot} (1+z)^{-3/2}, \end{aligned} \quad (7)$$

where $\epsilon_{k,0.05} \equiv \epsilon_k/0.05$ represents a typical efficiency factor of 5%.

3. THE HORIZON-AGN SIMULATION

The Horizon-AGN simulation (Dubois et al. 2014; see also Kaviraj et al. 2015, 2017) is a cosmological hydrodynamical simulation that uses the adaptive mesh refinement Eulerian hydrodynamics code RAMSES (Teyssier 2002). A complementary Horizon-noAGN simulation has also been performed that is identical to Horizon-AGN but has no prescription for black hole feedback. The simulation box is $100/h \text{ Mpc}$ comoving on each side, with 1024^3 dark matter particles at a mass resolution of $8 \times 10^7 M_\odot$. The simulation grid is refined throughout the simulation, with a maximum cell resolution of 1 physical kpc. Gas cools through emission by H, He, and metals (Sutherland & Dopita 1993), and is heated by a uniform UV background (Haardt & Madau 1996). Stars are created following a Poissonian random process (Dubois & Teyssier 2008) in gas denser than a hydrogen number density of 0.1 cm^{-3} following the Schmidt law, $\dot{\rho}_* = \epsilon_* \rho / t_{\text{ff}}$, where $\dot{\rho}_*$ is the star formation rate density, $\epsilon_* = 0.02$ is the star formation efficiency (Krumholz & Tan 2007), and the gas with density ρ has free-fall time $t_{\text{ff}} = \sqrt{3\pi/(32G\rho)}$ where G is the gravitational constant. The simulation uses a star particle mass resolution of $\approx 2 \times 10^6 M_\odot$. Stellar feedback is incorporated assuming a Salpeter (1955) initial mass function, with stellar winds and mechanical energy from Type II supernovae taken from STARBURST99 (Leitherer et al. 1999) and Type Ia supernova frequency taken from (Greggio & Renzini 1983).

AGN feedback in the Horizon-AGN simulation is modeled following Dubois et al. (2012). Black holes are seeded at $10^5 M_\odot$ when the gas mass density $\rho > \rho_0$, and the black hole accretion rate follows a Bondi-Hoyle-Lyttleton rate with an α boost factor (Booth & Schaye 2009) that scales as ρ^2 for $\rho > \rho_0$ and is 1 otherwise, accounting for high density gas that is not resolved in the simulation. The maximum accretion rate is set by the Eddington limit with a radiative efficiency of 0.1 (Shakura & Sunyaev 1973). When the accretion rate is high ($> 0.01 L_{\text{Edd}}$, following Merloni & Heinz 2008), a quasar-like feedback mode is assumed with 1.5% of the accretion energy injected as thermal energy in the surrounding gas (e.g. Booth & Schaye 2009). When the accretion rate is low ($< 0.01 L_{\text{Edd}}$), a radio feedback mode is assumed with bipolar jets at 10% efficiency, calibrated in Dubois et al. (2012). Feedback parameters are chosen to match the $M_{\text{BH}} - M_*$ (Häring & Rix 2004) and $M_{\text{BH}} - \sigma_*$ (Tremaine et al. 2002) relations observed at $z = 0$. Black hole sink particles merge when they are closer than 4 kpc and slower than their mutual escape velocity. A mock observational image of the Horizon-AGN simulation results showing a subset of the galaxies used in this work (green circles) is shown in Figure 1.

4. DATA

We use the Horizon-AGN (abbreviated here as “Y-AGN”) and Horizon-noAGN (abbreviated here as “N-AGN”) simulations for our simulated galaxy data, and make comparisons with observational measurements from Paper I (for clarity, hereafter “tSZ-SPT”) and Paper II (for clarity, hereafter “tSZ-ACT”). In order to obtain as robust of a galaxy sample as possible, we collect

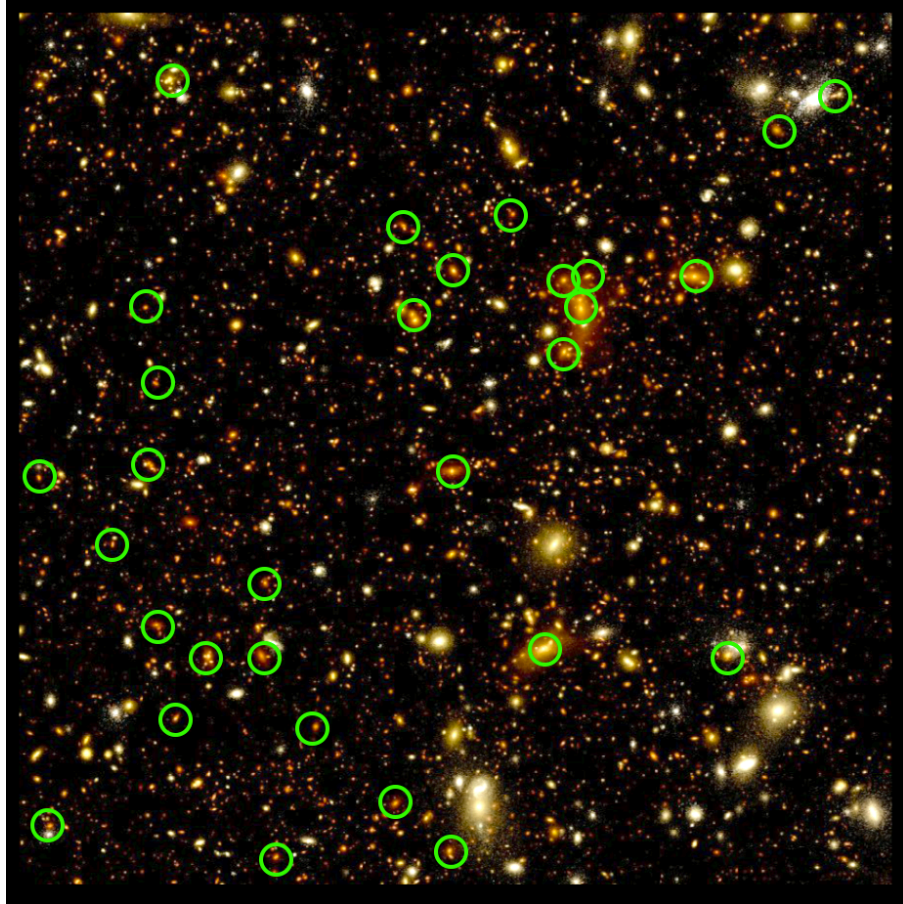


Figure 1. Adapted from Kaviraj et al. (2017), a 14 arcmin² simulated u, r, z image from the Horizon-AGN lightcone (Pichon et al. 2010). The 0.15 arcmin pixel⁻¹ resolution image is constructed from star particles within $0.1 < z < 5.8$. Select galaxies from the sample used in this work are annotated with green circles.

data from the full available spread of 18 equally-spaced redshift outputs between $z=0.5$ and 1.5. We initially find all galaxies in the simulations with at least 250 star particles at each redshift. We then extract various parameters for each galaxy (stellar mass, age, star formation rate, and active black hole flag in the Y-AGN case) and corresponding dark matter halo (total mass, gas mass, stellar mass, black hole mass, and dark matter mass) in both Y-AGN and N-AGN. The active black hole flag says that a black hole is active if its mass is greater than $10^6 M_\odot$ and its luminosity is greater than $0.01L_{\text{Edd}}$. The stellar mass is taken within a radius R_{200} , defined as the radius enclosing an overdensity of 200 times the critical density, given by

$$\frac{M(< R_{200})}{\frac{4}{3}\pi R_{200}^3} = 200\rho_c(z), \quad (8)$$

where $M(< R_{200})$ is the mass enclosed within R_{200} , and $\rho_c(z) = 3H^2(z)/(8\pi G)$.

We then perform a cut on the galaxies corresponding to the selection criteria in tSZ-SPT and tSZ-ACT, requiring $M_{\text{stellar}} \geq 10^{11} M_\odot$, $\text{Age} \geq 1$ Gyr, and a non-active black hole in the Y-AGN case. Although the simulation is periodic, we omit those few galaxies within 4.2 arcmin of the box edge to limit the computational overhead for correctly extracting the tSZ signal on the scales of ACT and SPT. The number of galaxies remaining in each red-

shift bin after the initial parameter cuts and the active black hole cut is shown in Figure 2. We also try using an age cut of $\text{Age} \geq 2$ Gyr to make sure that our results are not significantly biased by the cut on age, and we find no significant change in the results except for an increase in the N-AGN, $z = 1.0 - 1.5$, SPT-matched signal that does not affect our analysis of the results.

Note that we see a steady decrease in the fraction of galaxies that are flagged as active as we decrease in redshift, generally $> 20\%$ for $1.0 < z < 1.5$ (25% mean) and $< 20\%$ for $0.5 < z < 1.0$ (15% mean). This makes sense, since $z \approx 2$ represents the peak of AGN activity, and it should decrease to lower z . The $0.7 < z < 0.8$ bin is the one outlier, with 42% of the galaxies flagged as active. This is due solely to the $z = 0.76$ data, which flagged 72% of its galaxies as active, much more than any of the other redshift bins. This does not have any major effect on our results, though, since the lower redshift galaxies are plentiful and the final tSZ-SPT and tSZ-ACT matching cuts are limited by the number of higher redshift galaxies.

For each galaxy, we use the electron pressure to compute Compton- y values (Equation 2) and then project these values into two dimensions, representing the signal that would be observed. We then select a square region around each galaxy and simulate measurements corresponding to the beam and pixel sizes in both tSZ-SPT and tSZ-ACT. For tSZ-SPT, we use regions that

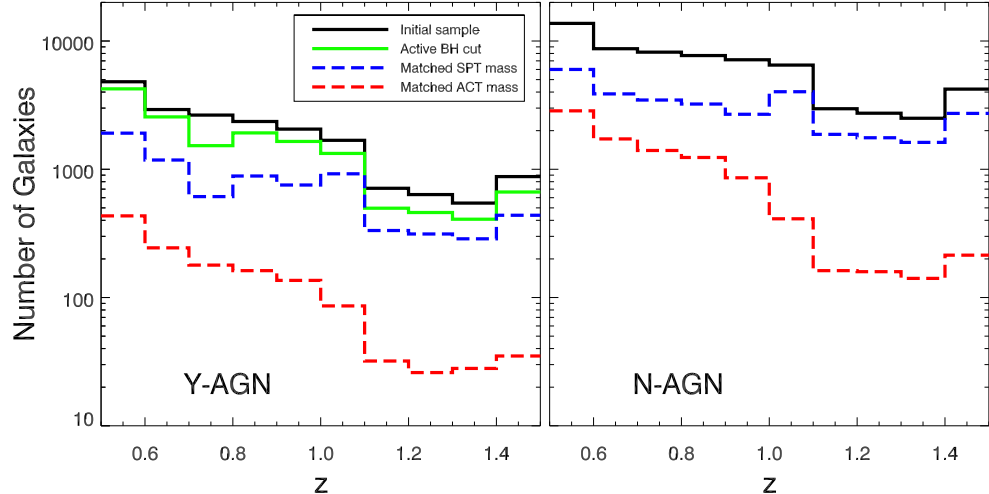


Figure 2. Number of galaxies per redshift bin for the initial population (black), after removing active black holes (green), and then after matching both the tSZ-SPT (blue dashed) and tSZ-ACT (red dashed) mass distributions. On the left is the Y-AGN simulation and on the right is the N-AGN simulation.

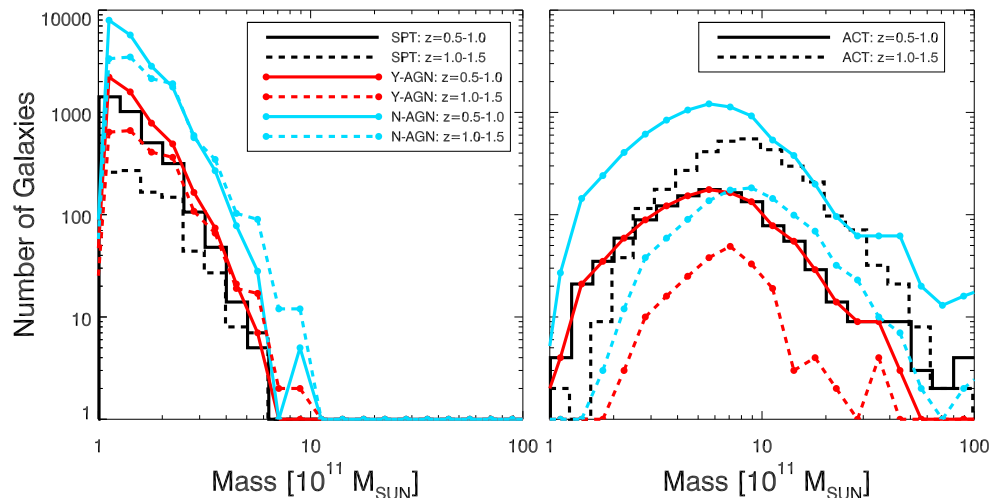


Figure 3. Mass selection comparisons. Solid lines represent the low- z sample and dashed lines represent the high- z sample. In the left plot, black represents the tSZ-SPT distribution, red represents the Y-AGN sample matched to tSZ-SPT, and light blue represents the N-AGN sample matched to tSZ-SPT. In the right plot, black represents the tSZ-ACT distribution, red represents the Y-AGN sample matched to tSZ-ACT, and light blue represents the N-AGN sample matched to tSZ-ACT.

are 8.25×8.25 arcmin, 33×33 pixels, convolved with a 1.15 arcmin FWHM Gaussian (corresponding to the 150 GHz SPT beam). For tSZ-ACT, we use regions that are 8.36×8.36 arcmin, 17×17 pixels, convolved with a 1.44 arcmin FWHM Gaussian (corresponding to the 148 GHz ACT beam). This results in a selection of galaxies for both Y-AGN and N-AGN at $0.5 < z < 1.5$ with tSZ measurements matching both tSZ-SPT and tSZ-ACT.

5. MEASUREMENTS

In order to compare the simulated and observed galaxies, we randomly build a population of simulated galaxies until their mass distribution matches the histogram distributions in tSZ-SPT and tSZ-ACT. The matched distribution is scaled by whichever bin has the lowest fraction of Horizon galaxies compared to that bin for tSZ-SPT or tSZ-ACT. These matched mass distributions are shown in Figure 3, where the left plot shows the Y-AGN (red) and N-AGN (blue) galaxies matched to tSZ-SPT, and the right plot shows them matched to tSZ-

ACT. Y-AGN and N-AGN galaxies are matched independently of one another since the matched properties can differ greatly between the two simulations. An issue arises since the tSZ-ACT mass distribution is skewed to higher masses while the overall Horizon distributions favor lower masses. This makes it difficult to match the tSZ-ACT distribution at the highest masses, so instead we choose some mass limit for each Horizon subset where we just keep all Horizon galaxies above that mass. This is especially clear for the Y-AGN $z = 1.0 - 1.5$ line in the right plot of Figure 3, where we only match the tSZ-ACT distribution up to $\approx 10^{12} M_\odot$ and keep every galaxy above that. In order to make sure that our results are insensitive to the random galaxy selection process, we run through several iterations of the process and find no significant change in the results.

The resulting tSZ-SPT, tSZ-ACT, and Horizon distributions for redshift and age are shown in Figure 4, the final number of Horizon galaxies at each redshift bin af-

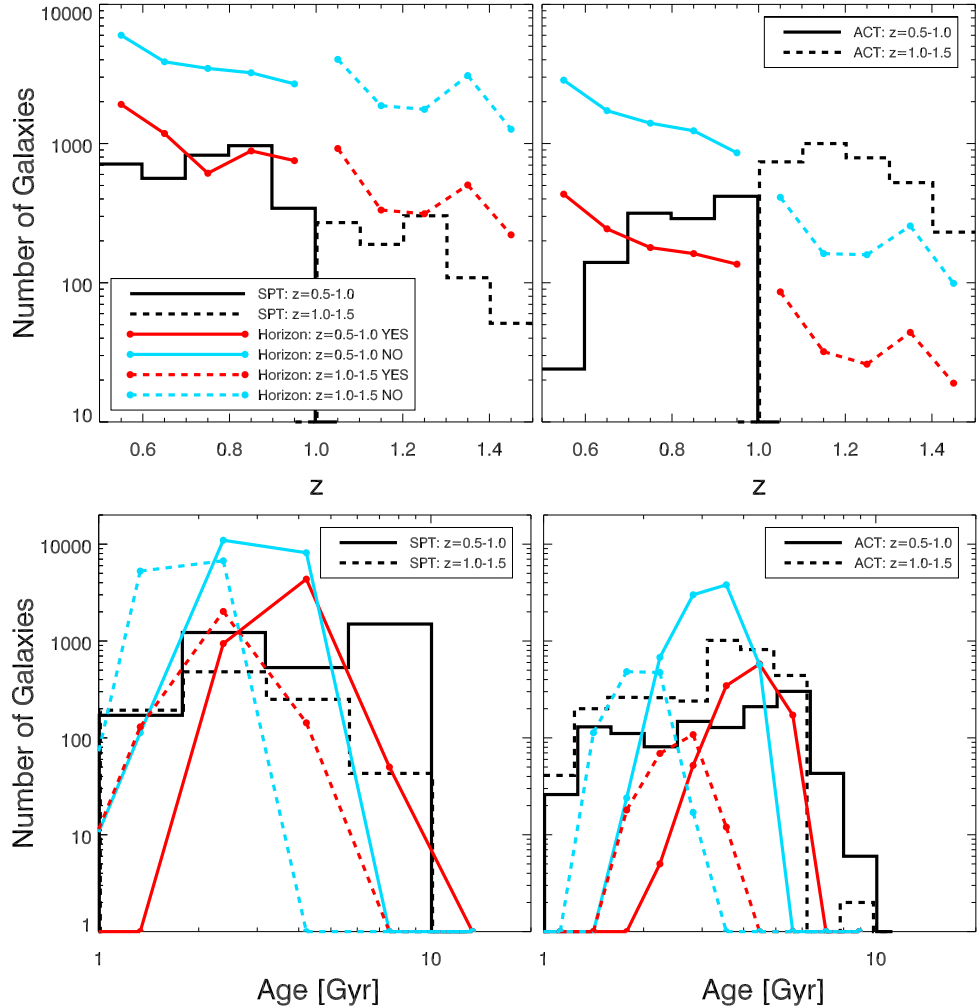


Figure 4. Redshift and age selection comparisons. The left plots are comparisons with SPT and the right plots are comparisons with ACT. The lines are the same as in Figure 3.

ter this matching are shown in Figure 2, and the final number of total galaxies in each redshift bin (“low- z ” is $0.5 < z < 1.0$ and “high- z ” is $1.0 < z < 1.5$) for each survey is given in Table 1. We note that the tSZ-SPT and tSZ-ACT numbers given in Table 1 represent the final measurements that incorporated Planck data, which used a smaller subset of galaxies than the original galaxy selection in tSZ-SPT and tSZ-ACT whose distributions are used in Figures 3 and 4. The additional galaxy cuts for the final measurements using Planck data were only spatially dependent, so we expect the mass, redshift, and age distributions to be roughly the same as those distributions in Figures 3 and 4. The tSZ measurement comparisons done in this work will use the Planck-incorporated tSZ-SPT and tSZ-ACT results.

The Horizon redshift distributions follow tSZ-SPT well, with the number of galaxies increasing with decreasing redshift. The Horizon redshift distributions do not follow tSZ-ACT as well, since tSZ-ACT peaks at higher masses (see Figure 3). Since mass tends to increase with decreasing redshift in the Horizon simulations, matching to the high tSZ-ACT masses results in a selection of lower redshift Horizon galaxies. The Horizon age distributions are similar to those from tSZ-SPT and tSZ-ACT, though N-AGN galaxies tend to be younger than Y-AGN galax-

Final bin:	Number	N(tSZ-SPT)	N(tSZ-ACT)
SPT low- z Y-AGN:	5345	937	-
SPT low- z N-AGN:	19249		
SPT high- z Y-AGN:	2293	240	-
SPT high- z N-AGN:	12004		
ACT low- z Y-AGN:	1154	-	227
ACT low- z N-AGN:	8073		
ACT high- z Y-AGN:	207	-	529
ACT high- z N-AGN:	1087		

Table 1
Final number of galaxies in each redshift bin (“low- z ” = $0.5 < z < 1.0$ and “high- z ” = $1.0 < z < 1.5$) for each corresponding survey, compared with the numbers from tSZ-SPT and tSZ-ACT that included Planck contamination modeling.

ies because star formation proceeds in N-AGN while it is quenched by the feedback in Y-AGN.

A comparison of averaged parameters from tSZ-SPT and tSZ-ACT with the final Horizon galaxies is shown in Table 2. Notice that the average redshifts of the Horizon galaxies are very close to the corresponding tSZ-SPT and tSZ-ACT bins except for the tSZ-ACT low- z bin. The tSZ-ACT low- z distribution drops off towards $z = 0.5$ due to the selection method used, while the Horizon galaxies increase towards lower z because only the mass distributions were matched, and higher mass galax-

Survey	z	$\langle z \rangle$	$\langle l_{\text{ang}}^2 \rangle$ (Gpc 2)	$\langle M \rangle$ ($10^{11} M_{\odot}$)	$\langle \text{Age} \rangle$ (Gyr)	$\langle z \rangle_M$	$\langle l_{\text{ang}}^2 \rangle_M$ (Gpc 2)	Y (10^{-7}Mpc^2)
SPT	0.5-1.0	0.72	2.30	1.51	4.34	0.72	2.30	$2.3^{+0.9}_{-0.7}$
Y-AGN SPT	0.5-1.0	0.70	2.22	1.52	3.91	0.70	2.23	2.67
N-AGN SPT	0.5-1.0	0.71	2.26	1.52	3.05	0.70	2.25	1.05
SPT	1.0-1.5	1.17	3.02	1.78	2.64	1.19	3.03	$1.9^{+2.4}_{-2.0}$
Y-AGN SPT	1.0-1.5	1.20	3.04	1.72	2.46	1.20	3.03	3.05
N-AGN SPT	1.0-1.5	1.22	3.05	1.72	1.85	1.22	3.05	0.79
ACT	0.5-1.0	0.83	2.56	7.81	3.80	0.86	2.61	$1.2^{+1.4}_{-1.4}$
Y-AGN ACT	0.5-1.0	0.69	2.21	7.00	4.25	0.69	2.20	10.82
N-AGN ACT	0.5-1.0	0.69	2.22	8.10	3.22	0.69	2.22	2.26
ACT	1.0-1.5	1.20	3.04	10.1	3.56	1.21	3.05	$1.9^{+1.1}_{-1.0}$
Y-AGN ACT	1.0-1.5	1.19	3.02	7.67	2.59	1.18	3.02	17.96
N-AGN ACT	1.0-1.5	1.20	3.04	10.30	1.96	1.19	3.03	4.01

Table 2

Mean ($\langle x \rangle$) and mass-averaged ($\langle x \rangle_M$) values for several relevant galaxy parameters, comparing tSZ-SPT and tSZ-ACT with the matched Horizon galaxies.

ies tend to exist at lower redshifts. The average masses are all very similar except for the Y-AGN tSZ-ACT case, which struggles to match the high redshift distribution of tSZ-ACT with its limited number of galaxies. tSZ-SPT and tSZ-ACT galaxies tend to be older than the Horizon galaxies, again except for the Y-AGN tSZ-ACT case, which has older galaxies due to its greater number of low redshift galaxies compared to tSZ-ACT.

When compared to low- z tSZ-SPT, the Y-AGN Y value is high by 0.4σ , while the N-AGN value is low by 1.8σ . For high- z tSZ-SPT, the Y-AGN value is high by 0.5σ while the N-AGN value is low by 0.6σ . When compared to low- z tSZ-ACT, the Y-AGN value is high by 6.9σ while the N-AGN value is high by 0.8σ . For high- z tSZ-ACT, the Y-AGN value is high by 14.6σ while the N-AGN value is high by 1.9σ . Given this, it appears that the Y-AGN model of AGN feedback decreases the tension between the simulated and observed tSZ measurements for low- z SpSPT, while the high- z tSZ-SPT results do not distinguish between the models. On the other hand, both the low- z and high- z tSZ-ACT results heavily disfavor the Y-AGN model of AGN feedback. We note that these comparisons are simply using the observational results plus errors and not taking into account the dispersion of the simulation averages. The redshift bins used to compute the averages span large mass ranges and therefore have large dispersions in tSZ signal, and we feel they are not relevant to the analysis we are doing.

Final average stacked stamps for the tSZ-SPT redshift bins are shown in Figure 5 for Y-AGN and N-AGN, along with the initial stamps from tSZ-SPT 150 and 220 GHz with matching scales. Final average stacked stamps for the tSZ-ACT redshift bins are shown in Figure 6 for Y-AGN and N-AGN, along with the initial stamps from tSZ-ACT 148 and 220 GHz with matching scales. The scales for both figures are set by the highest and lowest pixels out of all four Horizon stamps. For tSZ-SPT, although the 220 GHz stamps are noisy, there is promise that the large 220 GHz signal, representing contamination, could produce a substantial tSZ decrement when removed from the 150 GHz stamps, especially at low- z where there is already a decrement. For tSZ-ACT, it is clear that the tiny 220 GHz contaminants cannot

account for the expected large tSZ decrement shown in the Y-AGN stamps. The low- z tSZ-SPT stamps also indicate a larger extent to the signal than for the high- z stamps, ≈ 5 arcmin compared to ≈ 3 arcmin. At an average low- z value of $z=0.7$, the ratio of physical size to angular size is 7.2 kpc/arcsec, while at an average high- z value of $z=1.2$ it is 8.4 kpc/arcsec. This means the signal represents ~ 1.5 Mpc at high- z and ~ 2.2 Mpc at low- z . The larger angular size of the signal at low- z is therefore only slightly due to observational effects and mostly due to the signal being physically larger in size, possibly due to longer adiabatic expansion timescales (on average these are 1.5 times longer at low- z). This effect is not seen as clearly for tSZ-ACT, possibly due to the pixels being twice as large, or the masses, and therefore signal, being ≈ 6 times as large. These stamps also indicate that the 1 arcmin radius measurement aperture might be too small to contain the full tSZ signal. The low- z tSZ-SPT stamps would have the full signal better contained within an aperture twice as large, while the high- z tSZ-SPT stamps would need a 1.5-1.75 arcmin radius aperture. The tSZ-ACT stamps appear to need a 1.5-2 arcmin radius aperture to contain the full signal.

Mass binned averages of \tilde{Y} for three redshifts spanning the full range comparing Horizon to the model predictions are shown in Figure 7. There are several trends to notice here. The best-fit (using χ^2 analysis) linear log-log slopes and their associated 1σ levels for $z = (0.52, 1.03, 1.49)$ are $(1.1 \pm 0.2, 1.3 \pm 0.1, 1.3 \pm 0.1)$, respectively, for Y-AGN, and $(0.4 \pm 0.1, 0.8 \pm 0.1, 0.8 \pm 0.1)$ for N-AGN. Thus the Y-AGN and N-AGN curves roughly follow the $\tilde{Y} \propto Y \propto E_{\text{therm}} \propto M_{\star}$ relation indicated by the simple models in Equations (6) and (7), except for the lowest redshift of $z = 0.52$. For the first four mass bins at $z = 0.52$ (representing $\approx 1 \times 10^{11} - 6 \times 10^{11} M_{\odot}$) the best-fit slopes are 0.2 ± 0.2 for Y-AGN and 0.1 ± 0.1 for N-AGN. For this lowest redshift bin, \tilde{Y} appears to stay nearly flat for the lower masses. The Y-AGN and N-AGN curves also stay roughly the same distance apart, with average vertical log distances between the Y-AGN and N-AGN lines of 0.7 ± 0.2 at both $z = 1.03$ and 1.49 . At the highest redshift, the N-AGN line falls right on the model prediction with an average vertical difference of 0.02 ± 0.09 ,

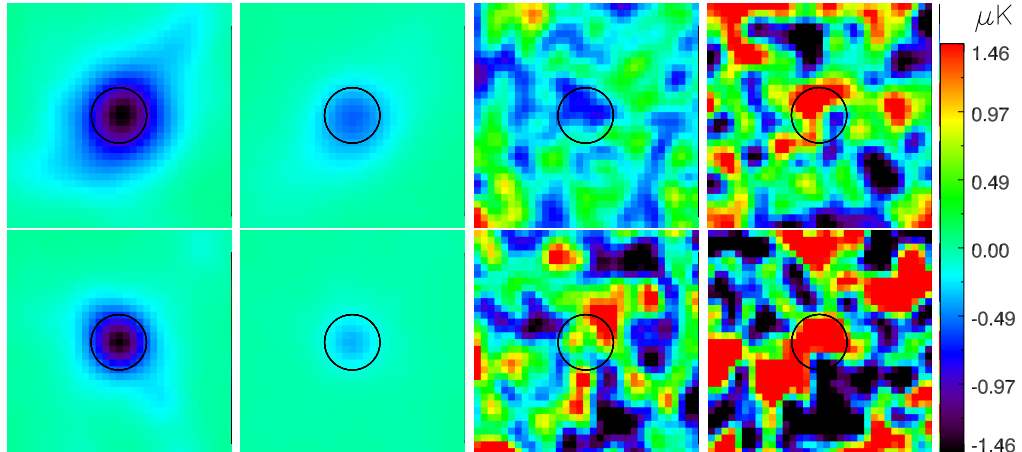


Figure 5. tSZ-SPT-matched 150 GHz stacked averages around galaxies for Y-AGN (left), N-AGN (left middle), low- z (top), and high- z (bottom). On the right are the initial tSZ-SPT stacking results with the same scale, for 150 GHz (right middle) and 220 GHz (right). Black circles represent a 1 arcmin radius.

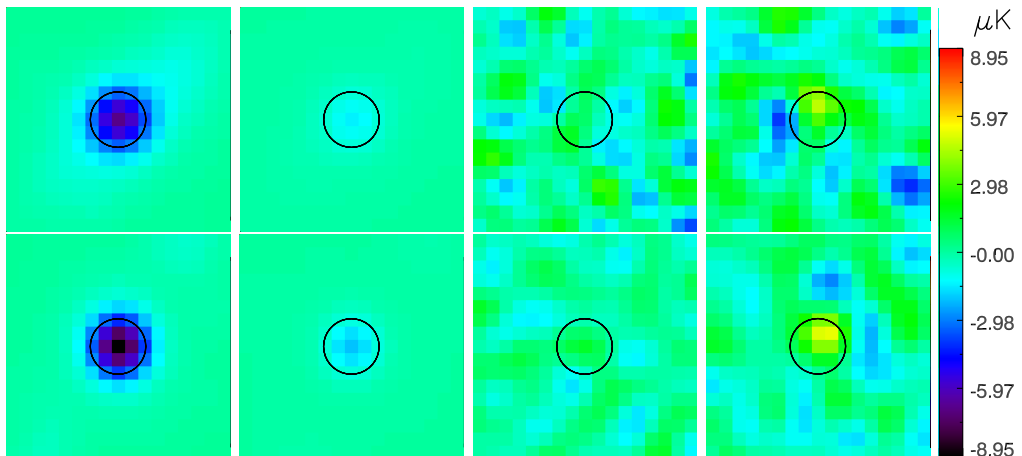


Figure 6. tSZ-ACT-matched 148 GHz stacked averages around galaxies for Y-AGN (left), N-AGN (left middle), low- z (top), and high- z (bottom). On the right are the initial tSZ-ACT stacking results with the same scale, for 148 GHz (right middle) and 220 GHz (right). Black circles represent a 1 arcmin radius.

while the Y-AGN line is considerably higher than the model prediction with an average vertical difference of 0.5 ± 0.1 . It is possible that this discrepancy is due to the Horizon AGN feedback prescription using more powerful feedback than the actual feedback processes happening in the observed galaxies (e.g. longer feedback times, multiple feedback episodes, overly powerful radio-mode jets). The simulated \tilde{Y} values then both drop relative to the models as the redshift decreases, likely due to longer cooling times, which the models do not account for.

Final mass-binned averages of \tilde{Y} for each redshift bin with each telescope, compared to the model predictions and the tSZ-SPT and tSZ-ACT results, are shown in Figure 8. Here we see that there is not a clear redshift dependence as predicted by the models, and the high- z values appear to be larger more often than the low- z values, contrary to the model predictions. This may be due to the fact that the curves are averaged over a range of redshifts, as well as the possibility of different behavior due to radiative cooling. Looking at the final measurements from tSZ-SPT and tSZ-ACT, we see as expected that the tSZ-SPT measurements (solid black circle/square) are consistent with the Y-AGN curves, al-

though it is hard to rule out the N-AGN curves which are about 1σ away. On the other hand, the tSZ-ACT measurements (open black circle/square) are consistent with the N-AGN curves and not at all consistent with the Y-AGN curves.

We also potentially gain some insight on discrepancies between the observational results and the simple models by looking at the simulation results. The tSZ-SPT low- z results are higher than the simple AGN feedback model predicts, while the tSZ-ACT results are all lower than the simple gravitational model predicts. Interestingly, both of these trends are reproduced in the Horizon results. This further suggests that the simple models are lacking in details that the Horizon simulations have incorporated, pointing to the usefulness of using detailed numerical simulations in this analysis.

6. DISCUSSION

In this work, we have taken the large-scale cosmological hydrodynamical simulation Horizon-AGN, with AGN feedback, and its counterpart Horizon-NoAGN, without AGN feedback, and extracted a sample of galaxies that match those from Papers I and II. We have then per-

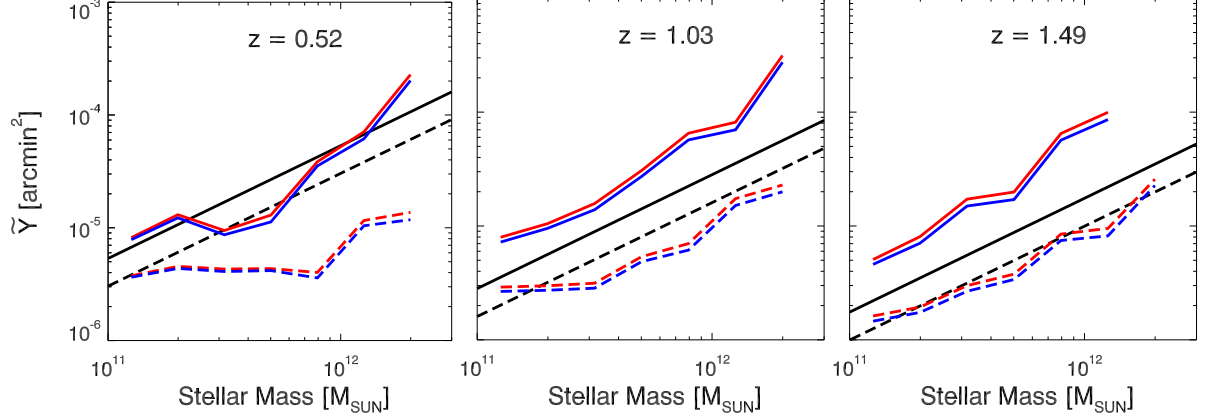


Figure 7. Comparison between scaled angularly-integrated, mass-binned Compton- γ measurements at a subset of simulation redshifts. Red lines are SPT-matched, blue are ACT-matched, solid are Y-AGN, and dashed are N-AGN. The solid black lines show Equation (6) + Equation (7) for the corresponding masses and redshifts, representing the simple AGN feedback energy model, and the dashed black lines show just Equation (6), representing only gravitational heating.

formed the same stacking procedure as tSZ-SPT and tSZ-ACT, measuring the tSZ effect by redshift, mass, and telescope survey. Our results can be summarized as follows:

(i) Low- z galaxies (i.e. $0.5 < z < 1.0$) appear to have a tSZ signal with significantly more angular extent than high- z galaxies ($1.0 < z < 1.5$). This phenomenon seems to be dominated by an increase in the physical size of the signal, rather than by observational effects due to physical sizes corresponding to larger angular sizes at lower redshifts. This increase in the physical size of the signal may be due to lower redshift galaxies having existed for a longer time since the peak of AGN activity than higher redshift galaxies, giving hot gas impacted by AGN feedback more time to expand and cool.

(ii) The aperture size of 1 arcmin appears to poorly capture the total stacked tSZ signal in both redshift bins and both Y-AGN and N-AGN simulations. This means less data (i.e. pixels with our signal of interest) and therefore a less statistically robust result than could be possible with a larger aperture. An aperture of 1.5-2.0 arcmin radius would be more effective in capturing the full signal, but would not be too large as to excessively increase the noise.

(iii) At low redshifts ($z \approx 0.52$), both the Y-AGN and N-AGN \tilde{Y} measurements appear to be flat with respect to mass at low masses ($M \lesssim 10^{12} M_\odot$), especially N-AGN. This is not predicted by the simple models.

(iv) At high redshift ($z = 1.49$) the N-AGN \tilde{Y} curve follows the model very well, while the Y-AGN curve is significantly higher than the model predicts. This is likely due to the differences in how the simple model and Horizon-AGN account for the amount of AGN feedback energy, either in magnitude or in duration.

(v) Both the Y-AGN and N-AGN \tilde{Y} curves appear to systematically drop relative to the model predictions as the redshift decreases. This is likely due to the models not taking into account the radiative cooling of the galaxies and surrounding gas, which would lower the tSZ signal, and which would increase in magnitude at lower redshifts as gas has longer to cool.

(vi) The models predict a distinct increase in \tilde{Y} going from high- z to low- z , while the Horizon measurements

show either no redshift dependence, or perhaps even an opposite effect where \tilde{Y} increases going from low- z to high- z . The simple models, as expected, do not capture the full energy dynamics over time. Furthermore, the Horizon results match trends seen in the observational measurements when compared to the simple models: the tSZ-SPT low- z results are higher than the simple AGN feedback model, and the tSZ-ACT high- z results are lower than the gravitational heating only model.

(vii) The tSZ-SPT results are consistent with the Y-AGN curves and inconsistent with the N-AGN curves at around a 1σ level, while the tSZ-ACT results are consistent with the N-AGN curves and inconsistent with the Y-AGN curves at $\gtrsim 7\sigma$.

Overall, it appears that the tSZ-SPT results suggest the presence of AGN feedback (although not very strongly), while the tSZ-ACT results strongly indicate that AGN feedback has little impact on the surrounding environment. These differing results could be due to the differences in galaxy selection, redshift, mass, age distribution, and contamination removal. It could also be possible that, with more precise measurements in the tSZ-SPT work regime (e.g. lower mass, lower redshift), we would find a trend similar to the tSZ-ACT results. These results suggest that the impact of AGN feedback on the energy around galaxies is significantly over-estimated by the Horizon-AGN simulation and likely other simulations that employ strong AGN feedback, at least for higher-mass ($\gtrsim 5 \times 10^{11} M_\odot$) galaxies (keeping in mind that AGN models vary significantly between different simulations). These comparisons are unprecedented in their attempt to measure the tSZ effect around moderate redshift elliptical galaxies using the first publicly available data from the SPT and ACT surveys, and there remain many open questions that should be investigated regarding these tSZ stacking measurements, as indicated by many of the above summary points.

Thus, there is a lot of further work to be done in the near future on these measurements. It may be interesting to investigate redshifts lower than 0.5 and higher than 1.5, as well as different cuts on galaxy parameters, to see if improvements can be made in these tSZ stacks, and to understand the overall evolution of the hot gas around galaxies. In addition to the stellar mass of galaxies, it

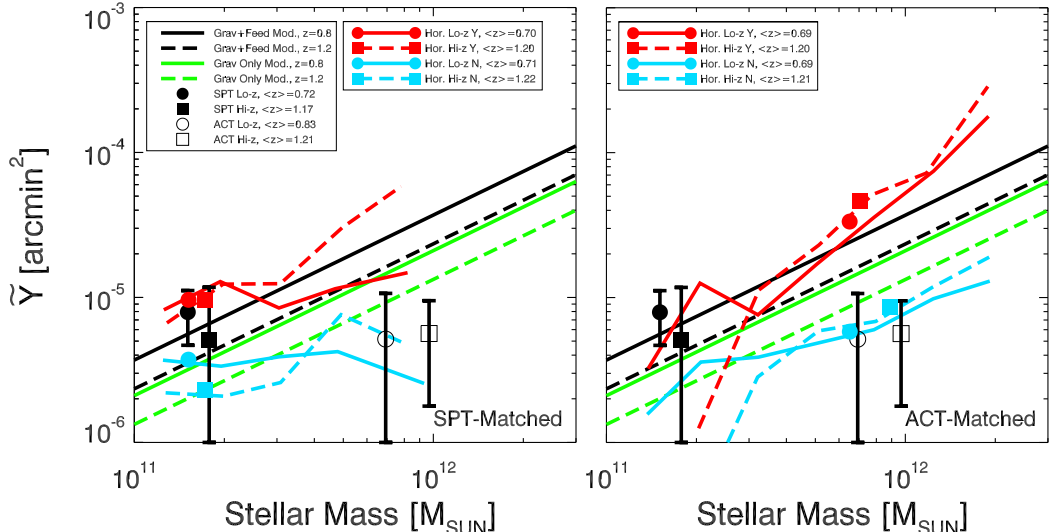


Figure 8. Final matched stack values for SPT and ACT. For all lines, solid is low- z ($z = 0.5 - 1.0$) and dashed is high- z ($z = 1.0 - 1.5$). For the points, circles are low- z and squares are high- z . Black and green lines show the simple models with and without feedback, respectively. Solid black points show the tSZ-SPT results, and open black points show the tSZ-ACT results. Red shows the Horizon-AGN results and blue shows the Horizon-NoAGN results, matched to tSZ-SPT in the left plot and tSZ-ACT in the right plot.

could be useful to explore relations between dark matter halo masses and the tSZ effect. This work could also be expanded by doing similar simulations to Horizon-AGN but using various models of AGN feedback, in order to understand a much more detailed picture of the AGN feedback process that is giving the observational results. In fact, a new zoomed subset of the Horizon-AGN simulation has been produced with a maximum resolution of 40 pc instead of 1 kpc, necessarily requiring a new AGN feedback prescription. This could provide further interesting comparisons, and with these important large-scale cosmological simulations with AGN feedback continuing to be produced, it is now time for more comparisons and analyses similar to what is done in this work.

Finally, there are several next-generation CMB detectors currently running, and planned, that are potentially releasing data soon. This includes ACTPol (Niemack et al. 2010), Advanced ACTPol (Calabrese et al. 2014), SPT-Pol (Austermann et al. 2012), SPT-3G (Benson et al. 2014), and LiteBIRD (Matsumura et al. 2014), which have a large increase in sensitivity as well as more frequency bands compared to the ACT and SPT data used in the tSZ-ACT and tSZ-SPT work. These will give much better tSZ measurements, while the extra frequency bands would improve the ability to deal with contamination in the tSZ signal. The TolTEC camera (<http://toltec.astro.umass.edu/>) on the Large Millimeter Telescope will measure the microwave sky at much higher angular resolution, helping to distinguish between models not only by the overall magnitude of the tSZ effect, but also by the overall profile on the sky. These measurements can then provide future simulation work with even more robust observations to compare with, leading to increasingly constrained results.

We would like to generously thank Clotilde Laigle for making the beautiful Horizon-AGN mock lightcone image. AS would like to thank Julien Devriendt and the University of Oxford Sub-department of Astrophysics for hosting him where a significant part of this work was carried out. He would also like to thank the

ASU Graduate and Professional Student Association for funding part of this visit through their travel grant program. This work has made use of the Horizon Cluster, hosted by Institut d’Astrophysique de Paris, and data from the Horizon simulations (www.horizon-simulation.org/about.html), with generous help from Stephane Rouboro. We would also like to thank the COSMOS2015 team for allowing us to use their data ahead of publication. This work is part of the Horizon-UK project. AS and ES were supported by the National Science Foundation under grant AST14-07835.

REFERENCES

Austermann, J. E., Aird, K. A., Beall, J. A., et al. 2012, in Proc. SPIE, Vol. 8452, Millimeter, Submillimeter, and Far-Infrared Detectors and Instrumentation for Astronomy VI, 84521E

Benson, B. A., Ade, P. A. R., Ahmed, Z., et al. 2014, in Proc. SPIE, Vol. 9153, Millimeter, Submillimeter, and Far-Infrared Detectors and Instrumentation for Astronomy VII, 91531P

Booth, C. M., & Schaye, J. 2009, MNRAS, 398, 53

Calabrese, E., Hložek, R., Battaglia, N., et al. 2014, J. Cosmology Astropart. Phys., 8, 010

Cen, R., & Safarzadeh, M. 2015, ApJL, 809, L32

Chatterjee, S., Di Matteo, T., Kosowsky, A., & Pelupessy, I. 2008, MNRAS, 390, 535

Chatterjee, S., Ho, S., Newman, J. A., & Kosowsky, A. 2010, ApJ, 720, 299

Cowie, L. L., Songaila, A., Hu, E. M., & Cohen, J. G. 1996, AJ, 112, 839

Crichton, D., Gralla, M. B., Hall, K., et al. 2016, MNRAS, 458, 1478

Croton, D. J., Springel, V., White, S. D. M., et al. 2006, MNRAS, 365, 11

da Silva, A. C., Barbosa, D., Liddle, A. R., & Thomas, P. A. 2000, MNRAS, 317, 37

Dolag, K., Komatsu, E., & Sunyaev, R. 2016, MNRAS, 463, 1797

Drory, N., & Alvarez, M. 2008, ApJ, 680, 41

Dubois, Y., Devriendt, J., Slyz, A., & Teyssier, R. 2012, MNRAS, 420, 2662

Dubois, Y., & Teyssier, R. 2008, A&A, 477, 79

Dubois, Y., Pichon, C., Welker, C., et al. 2014, MNRAS, 444, 1453

Fabian, A. C. 2012, ARA&A, 50, 455

Ferrarese, L. 2002, *ApJ*, 578, 90

Gralla, M. B., Crichton, D., Marriage, T. A., et al. 2014, *MNRAS*, 445, 460

Granato, G. L., De Zotti, G., Silva, L., Bressan, A., & Danese, L. 2004, *ApJ*, 600, 580

Greco, J. P., Hill, J. C., Spergel, D. N., & Battaglia, N. 2015, *ApJ*, 808, 151

Greggio, L., & Renzini, A. 1983, *A&A*, 118, 217

Haardt, F., & Madau, P. 1996, *ApJ*, 461, 20

Hand, N., Appel, J. W., Battaglia, N., et al. 2011, *ApJ*, 736, 39

Häring, N., & Rix, H.-W. 2004, *ApJL*, 604, L89

Hirschmann, M., Somerville, R. S., Naab, T., & Burkert, A. 2012, *MNRAS*, 426, 237

Hobson, M. P., & Magueijo, J. 1996, *MNRAS*, 283, 1133

Hojjati, A., McCarthy, I. G., Harnois-Déraps, J., et al. 2015, *J. Cosmology Astropart. Phys.*, 10, 047

Hojjati, A., Tröster, T., Harnois-Déraps, J., et al. 2016, *ArXiv e-prints*, arXiv:1608.07581

Hopkins, P. F., Richards, G. T., & Hernquist, L. 2007, *ApJ*, 654, 731

Kaviraj, S., Devriendt, J., Dubois, Y., et al. 2015, *MNRAS*, 452, 2845

Kaviraj, S., Laigle, C., Kimm, T., et al. 2017, *MNRAS*, 467, 4739

Krumholz, M. R., & Tan, J. C. 2007, *ApJ*, 654, 304

Lapi, A., Raimundo, S., Aversa, R., et al. 2014, *ApJ*, 782, 69

Leitherer, C., Schaerer, D., Goldader, J. D., et al. 1999, *ApJS*, 123, 3

Marconi, A., & Hunt, L. K. 2003, *ApJL*, 589, L21

Matsumura, T., Akiba, Y., Borill, J., et al. 2014, *Journal of Low Temperature Physics*, 176, 733

Merloni, A., & Heinz, S. 2008, *MNRAS*, 388, 1011

Niemack, M. D., Ade, P. A. R., Aguirre, J., et al. 2010, in *Proc. SPIE*, Vol. 7741, Millimeter, Submillimeter, and Far-Infrared Detectors and Instrumentation for Astronomy V, 77411S

Pichon, C., Thiébaut, E., Prunet, S., et al. 2010, *MNRAS*, 401, 705

Planck Collaboration, Ade, P. A. R., Aghanim, N., et al. 2013, *A&A*, 557, A52

—. 2016, *A&A*, 586, A140

Rees, M. J., & Ostriker, J. P. 1977, *MNRAS*, 179, 541

Refregier, A., Komatsu, E., Spergel, D. N., & Pen, U.-L. 2000, *Phys. Rev. D*, 61, 123001

Reichardt, C. L., Stalder, B., Bleem, L. E., et al. 2013, *ApJ*, 763, 127

Roncarelli, M., Moscardini, L., Borgani, S., & Dolag, K. 2007, *MNRAS*, 378, 1259

Ruan, J. J., McQuinn, M., & Anderson, S. F. 2015, *ApJ*, 802, 135

Salpeter, E. E. 1955, *ApJ*, 121, 161

Scannapieco, E., & Oh, S. P. 2004, *ApJ*, 608, 62

Scannapieco, E., Thacker, R. J., & Couchman, H. M. P. 2008, *ApJ*, 678, 674

Scaramella, R., Cen, R., & Ostriker, J. P. 1993, *ApJ*, 416, 399

Schaan, E., Ferraro, S., Vargas-Magaña, M., et al. 2016, *Phys. Rev. D*, 93, 082002

Seljak, U., Burwell, J., & Pen, U.-L. 2001, *Phys. Rev. D*, 63, 063001

Shakura, N. I., & Sunyaev, R. A. 1973, *A&A*, 24, 337

Shankar, F., Weinberg, D. H., & Miralda-Escudé, J. 2013, *MNRAS*, 428, 421

Shankar, F., Bernardi, M., Sheth, R. K., et al. 2016, *MNRAS*, 460, 3119

Sijacki, D., Springel, V., Di Matteo, T., & Hernquist, L. 2007, *MNRAS*, 380, 877

Soergel, B., Flender, S., Story, K. T., et al. 2016, *MNRAS*, 461, 3172

Spacek, A., Scannapieco, E., Cohen, S., Joshi, B., & Mauskopf, P. 2016, *ApJ*, 819, 128

—. 2017, *ApJ*, 834, 102

Springel, V., White, M., & Hernquist, L. 2001, *ApJ*, 549, 681

Sunyaev, R. A., & Zeldovich, Y. B. 1972, *Comments on Astrophysics and Space Physics*, 4, 173

Sutherland, R. S., & Dopita, M. A. 1993, *ApJS*, 88, 253

Teyssier, R. 2002, *A&A*, 385, 337

Thacker, R. J., Scannapieco, E., & Couchman, H. M. P. 2006, *ApJ*, 653, 86

Tremaine, S., Gebhardt, K., Bender, R., et al. 2002, *ApJ*, 574, 740

White, S. D. M., & Frenk, C. S. 1991, *ApJ*, 379, 52

Zhang, P., Pen, U.-L., & Wang, B. 2002, *ApJ*, 577, 555